Progress In Electromagnetics Research M, Vol. 109, 137–148, 2022

Development of Ground-Based SFCW-ArcSAR System and Investigation on Point Target Response

Zhuoyan Gao[1, 2], Yan Jia[1, 2], Shuyi Liu[1, 2], and Xiangkun Zhang[1, 2, *]

Abstract—Arc synthetic aperture radar (ArcSAR) forms the synthetic aperture through uniform circular motion with antenna pointed outwards circular trajectory, so the point target response is different from traditional linear SAR and Circular SAR (CSAR). Due to the unique imaging mode, ArcSAR has the characteristics of large field of view and constant azimuth angular resolution. The ArcSAR system is built by vector network analyzer (VNA), rotating platform, standard gain horn antenna, and computer, and the system transmits stepped frequency continuous wave (SFCW). A Qt-based graphical user interface (GUI) is designed to realize the accurate and convenient remote control of the system. An outdoor imaging experiment was carried out with a corner reflector to investigate the point target response of SFCW-ArcSAR which has unique forms in Cartesian coordinate and cylindrical coordinate systems. In order to avoid the additional phase error introduced by coordinate transformation based on interpolation, back projection (BP) algorithm is applied in Cartesian coordinate system and cylindrical coordinate system, respectively. The point target response presents a 2-D sinc function in cylindrical coordinate system. The azimuth angular resolution is 0.0175 rad under the experimental condition of 1.9 m-rotating radius and 16° antenna beamwidth. The simulation results agree with measured ones, which prove the validity of SFCW-ArcSAR system and correctness of theoretical analysis. The imaging result based on BP algorithm and corner reflector can be used to evaluate other ArcSAR imaging algorithms.

1. INTRODUCTION

Ground-based synthetic aperture radar (GBSAR) can form a two-dimensional complex image of the observed scene. In the past two decades, GBSAR has received more and more attention, and multiple observation modes have been developed. Compared with airborne or spaceborne systems, GBSAR has a controllable motion track and higher repeatability for ground object observation, which is more suitable for long-term micro-deformation monitoring of artificial structure or natural environment [1–3]. Applications of GBSAR include but not limited to: landslides [4], open pit mines [5], glaciers [6], dams [7], volcanos [8], etc.

GBSAR can be classified into linear SAR, Arc synthetic aperture radar (ArcSAR) or multiple input multiple output (MIMO) according to the formation mode of synthetic aperture. Linear SAR is the most common type. Its antenna moves along a linear rail to form a synthetic aperture. Therefore, its field of view is limited by the length of the rail and the beamwidth of antenna. In order to improve the speed of acquisition, MIMO technology is developed [9, 10]. The acquisition time for each image is less than 40 milliseconds, and the large synthetic aperture is more easily to synthesize. Ground-based ArcSAR is a new imaging mode which forms the synthetic aperture by uniform circular motion. The antenna of circular SAR (CSAR) is pointed inwards to the center of the circular trajectory, which can observe the

Received 17 December 2021, Accepted 22 March 2022, Scheduled 1 April 2022

* Corresponding author: Xiangkun Zhang (zhangxiangkun@mirslab.cn).

[1] Key Lab of Microwave Remote Sensing, National Space Science Center, Chinese Academy of Sciences, Beijing 100190, China.

[2] School of Electronic, Electrical and Communication Engineering, University of Chinese Academy of Sciences, Beijing 100049, China.

target over a circular aperture and then realize the digital elevation model (DEM) reconstruction of the target [11, 12]. However, the antenna of ArcSAR is pointed outwards the circular trajectory, and the observation area formed on the ground is annulus. As a result of constant azimuth angular resolution and wide observation range of ArcSAR, it has unique application advantages.

Several institutions are currently working on ArcSAR systems. The only commercially available system is the IBIS-ArcSAR developed by IDS Georadar [13, 14]. The system transmits frequency modulated continuous wave (FMCW) and makes a 360° observation of the surrounding ground objects in 40 s. The system is also equipped with MIMO radar channel for DEM reconstruction. Lee et al. from Kangwon National University have developed an ArcSAR system mounted on a truck [15]. The system is mainly constructed by vector network analyzer (VNA). It transmits stepped frequency continuous wave (SFCW) and works at X-band. The arm length can be extended from 2.19 m to 4.19 m. There are two working modes: spot mode and scan mode. The coherent integral arc is longer, and azimuth resolution is finer under the spot mode. Luo et al. from the Institute of Electronics, Chinese Academy of Sciences built an ArcSAR system based on the self-developed MiniSAR and a rotating platform [16]. The system transmits FMCW signals and operates at X-band with arm lengths ranging from 1.5 m to 2.5 m. Interferometry experiments were carried out based on the system, and the deformation of landslide is obtained. Lin et al. from North China University of Technology built an FMCW ArcSAR system [17]. Different from the above three systems, the rotation plane is on the same plane with the target, which leads to different imaging geometries and imaging algorithms.

The National Space Science Center (NSSC) of Chinese Academy of Sciences has also engaged in the research of ArcSAR. A ground-based SFCW-ArcSAR system is constructed by a VNA, a rotating platform with a telescopic arm, and a computer. A Qt-based GUI makes the remote control of the system more convenient. BP algorithm [18–20] is applied in both Cartesian coordinate and cylindrical coordinate due to the unique signal characteristic of ArcSAR. The purpose of the paper is to have a clear research of the point target response of ArcSAR, and further applications can be realized based on this work. The experiment results can be used to facilitate the evaluation of other ArcSAR imaging algorithms proposed in the future.

The paper is organized as follows. Section 2 describes the configuration of SFCW-ArcSAR built by NSSC. In Section 3, signal model and signal properties of ArcSAR are analyzed. The ArcSARBP algorithm and simulation results in Cartesian coordinate system and cylindrical coordinate system are demonstrated in Section 4. The experimental results and point target analysis are presented Section 5.

2. CONFIGURATION OF ARCSAR

The SFCW-ArcSAR system works at Ku band and consists of VNA, antennas, rotating platform, and data processing computer. The VNA is placed on a platform at the pivot of the rotating platform and is connected with the computer through an Ethernet interface. Computer is used to send standard commands for programmable instruments (SCPI) to make VNA generate SFCW signal. The rotating platform is connected with the computer through an RS422 communication line. Computer sends control instructions to the rotating platform, so that the platform can realize a variety of rotating functions including timed step by step operation, single step operation, uniform rotation angle preset operation, etc. The angle positioning accuracy is less than 0.1°, and rotation speed error is less than 5%. There are two rotating arms with adjustable length of 1.5 m $\sim$ 2.5 m on the rotating platform. They have two functions: Change the azimuth angular resolution and form a specific baseline for interferometry measurement. Two standard gain horn antennas are mounted on the ends of the rotating arms to implement the function of transmitting and receiving signals. The height of the rotating platform can also be increased or decreased in segments. The rotating platform and VNA are remote controlled based on Qt software and C++ programming language. The operations of equipment control, data storage, and data processing are integrated into the computer terminal, and a GUI is made to make the control of the experiment more convenient. Besides, a handheld laser rangefinder is used as a reference to evaluate the range measurement accuracy of the ArcSAR. The system configuration is shown in Fig. 1, and the main parameters of the system are shown in Table 1.

Table 1. Parameters of SFCW-ArcSAR.

Parameter	Value	Parameter	Value
Center freq.	16.15 GHz	Beamwidth	16°
Bandwidth	300 MHz	Polarization	HH
Step num.	301	Rotation radius	1.9 m
PRF	5 Hz	Height	34 m
Power	1 dBm	Angular velocity	0.5°/s
Target range	8 m	Field of view	60°

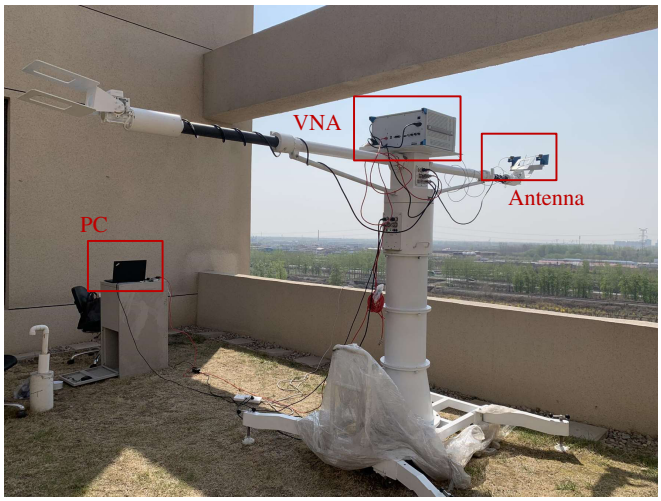

Figure 1. System configuration.

3. SIGNAL MODEL AND PROPERTIES

3.1. Signal Model

The observation geometry of ArcSAR is as follows.

From Fig. 2, the antenna of ArcSAR is attached to the end of the rotating arm with length of r_a. The other end of the rotating arm is fixed on the axis of rotation platform of height H. The angular velocity of antenna is ω, and azimuth coherent integral angle is $\theta = \omega\eta$. The rotation direction of antenna is azimuth, and the time is represented by η. Range time is represented by t. Supposing that there is an ideal point target P in the scene, the position can be expressed as $P(x_p, y_p)$ in Cartesian coordinates and $P(r_p, \theta_p)$ in cylindrical coordinates. The position at which the radar just illuminates the target is A, and the position at which the radar loses the sight of the target is B. The angle θ_{sys} between PA and PB is synthetic angle which is related to azimuth resolution. The beamwidth of antenna is θ_{BW}. When the target distance is much greater than the rotation radius, at A and B, the angle between beam center and target is approximately equal to $\theta_{BW}/2$. The nearest instant slant distance between antenna and point target is R_0; the distance from the rotation center O′ to the point target is R_c; and the pitch angle between the rotation plane and O′P is β.

According to Fig. 2, the instant slant distance between ArcSAR and point target in Cartesian coordinate can be described as:

$$R_1(\eta) = \sqrt{H^2 + (x_p - r_a\cos\omega\eta)^2 + (y_p - r_a\sin\omega\eta)^2} \tag{1}$$

$$\eta \in (\eta_A, \eta_B) \tag{2}$$

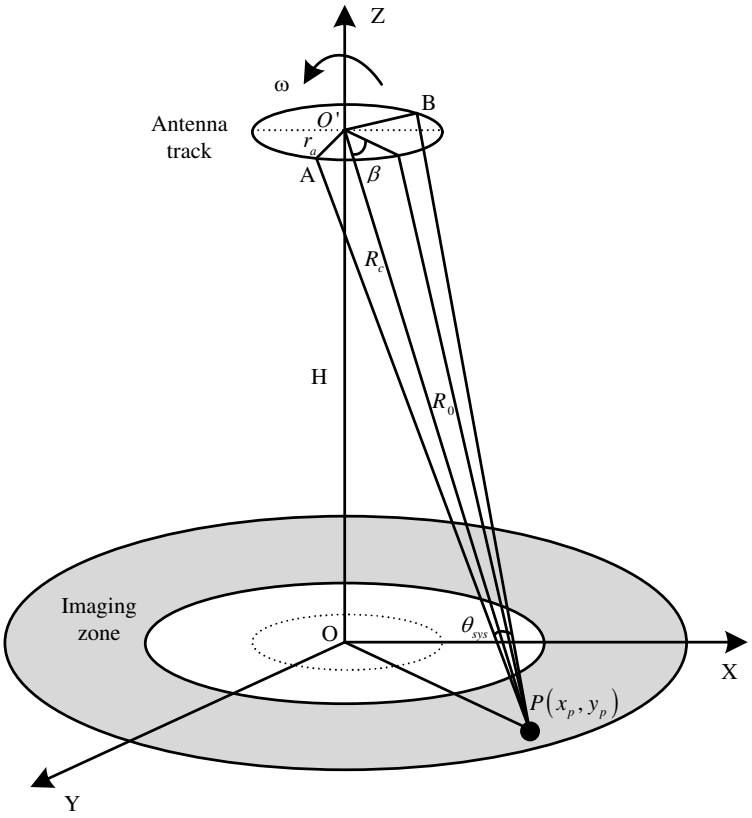

Figure 2. Observation geometry of ArcSAR.

The instant slant distance in cylindrical coordinate is:

$$R_2(\eta) = \sqrt{r_a^2 + R_c^2 - 2r_a R_c \cos(\omega\eta - \theta_p)\cos\beta} \tag{3}$$

$R_1(\eta)$ and $R_2(\eta)$ will be applied to BP algorithm in different coordinate systems. The radar system based on VNA transmits stepped frequency continuous wave (SFCW). Let the starting frequency be f_0 and frequency step increment be Δf. t represents the range time of the transmitted signal, and η represents the azimuth time. n is an integer between 0 and $N-1$, and N is the total number of stepped frequencies. Normalizing the amplitude, the transmitted signal is:

$$S_t(f,t) = \exp\left[2\pi(f_0 + n\Delta f)t\right] \tag{4}$$

Received signal is:

$$S_r(f,t,\eta) = \exp\left[2\pi(f_0 + n\Delta f)\left(t - 2R(\eta)/c\right)\right] \tag{5}$$

The intermediate frequency (IF) signal after orthogonal demodulation can be expressed as:

$$S_{IF}(f,\eta) = S_r(t) \otimes S_t(t) = \exp\left\{-j\frac{4\pi\left(f_0 + n\Delta f\right)R(\eta)}{c}\right\} \tag{6}$$

Inverse Fourier transform can be applied to IF signal to realize range compression [21]:

$$S(l,\eta) = \frac{1}{N}\frac{\sin\left[\pi\left(l - 2NR(\eta)\Delta f/c\right)\right]}{\sin\left[\pi/N\left(l - 2NR(\eta)\Delta f/c\right)\right]} \cdot \exp\left(-j4\pi f_0 R(\eta)/c\right) \cdot \exp\left[j\frac{(N-1)\pi l}{N}\right] \tag{7}$$

where l is the range sample. The signal in Eq. (7) is a sinc function in the time domain, so range compression is realized, and BP algorithm can be further applied to form radar image.

3.2. Range Resolution

Range resolution of ArcSAR is the same as linear SAR, which is related to the bandwidth of the transmitted signal. Without windowing, range resolution is:

$$\delta_r = 0.886 \cdot \frac{c}{2N\Delta f} \tag{8}$$

3.3. Azimuth Resolution

Azimuth resolution is the parameter that we focus on. Targets located in the same distance and at different azimuth angles have the same Doppler histories, namely the azimuth angular shift invariant and range shift variant property. So, taking point $P(R_c, 0)$ as an example, the angular resolution derivation schematic diagram is shown in Fig. 3.

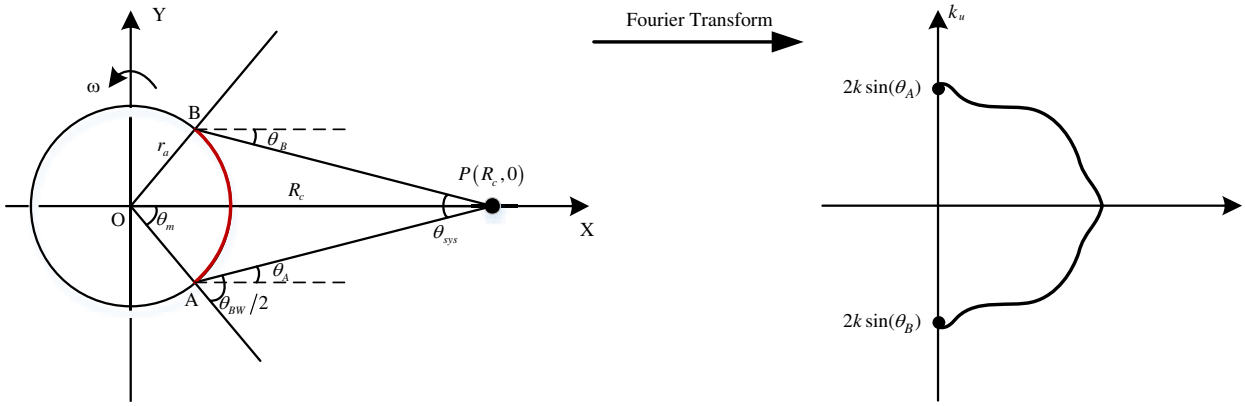

Figure 3. Angular resolution derivation diagram of ArcSAR.

Aspect angle is represented by θ_n, and the wave number in azimuth is [22]:

$$k_u = 2k \cdot \sin(\theta_n) \tag{9}$$

where $k = 2\pi/\lambda$. The antenna moves from A to B, generating a Doppler bandwidth of:

$$\Omega = k_u(\theta_A) - k_u(\theta_B) = 4k \sin(\theta_{sys}/2) \tag{10}$$

So, the azimuth resolution in the dimension of range is:

$$\delta_a = \frac{2\pi}{|\Omega|} c = \frac{0.886 \cdot \lambda}{4 \cdot \sin(\theta_{sys}/2)} \tag{11}$$

where λ represents the wave length of center frequency. In the triangle OPA, based on the triangle sine theory, we can get [17]:

$$\frac{\sin(\theta_{sys}/2)}{r_a} = \frac{\sin(\theta_{BW}/2)}{R_c} \tag{12}$$

Substituting Eq. (12) into Eq. (11), the azimuth resolution is:

$$\delta_a = \frac{0.886 \cdot \lambda R_c}{4r_a \cdot \sin(\theta_{BW}/2)} \tag{13}$$

So, the azimuth angular resolution is derived:

$$\delta_\theta = \frac{0.886 \cdot \lambda}{4r_a \cdot \sin(\theta_{BW}/2)} \tag{14}$$

From Eq. (14), it is obvious that azimuth angular resolution of ArcSAR is invariant with range. The larger the length of the rotating arm and beamwidth are, the finer the azimuth resolution is.

4. ARCSAR-BP IMAGING ALGORITHM

4.1. Overview

BP algorithm is a time domain imaging algorithm. Although the processing efficiency is low, the imaging accuracy is relatively high. The raw data of ArcSAR can be imaged in different coordinates conveniently based on BP algorithm, so the phase error caused by coordinate transformation completed by interpolation can be avoided [23]. The amplitude of a certain pixel of radar complex image can be obtained by coherently accumulating the signal history of the pixel [24]:

$$I(j,k) = \sum_i S(l,i,N_f) \cdot \exp(j4\pi R_{(j,k),i}/\lambda) \tag{15}$$

where $S(l,i,N_f)$ is the range compressed data, and N_f represents the interpolation multiple in range. i indicates the index of the antenna position, with a total number of N_i; j is the index of x-axis; k is the index of y-axis of imaging grid.

First of all, in order to obtain a more accurate imaging result, the raw data should be interpolated in the range. Since raw data is obtained in range frequency domain, zero padding can be applied to raw data conveniently in order to smooth the subsequent interpolation of BP algorithm [25]. Then the imaging domain is discretized, and imaging grid $I(j,k)$ is set up. The spacing of the grid should be smaller than the radar resolution. The distance $R_{(j,k),i}$ between imaging grid $I(j,k)$ and every antenna position i is calculated, and the corresponding data is calculated through sinc interpolation. For each interpolated data $S(l,i,N_f)$, compensating phase related to $R_{(j,k),i}$ is multiplied and then add the compensated data to the data relative to $i-1$ position. The value of certain pixel can be obtained through N_i iterations and summation. Finally, the radar image $I(j,k)$ is formed by iterating the whole imaging grid. The diagram of ArcSAR-BP algorithm is shown in Fig. 4.

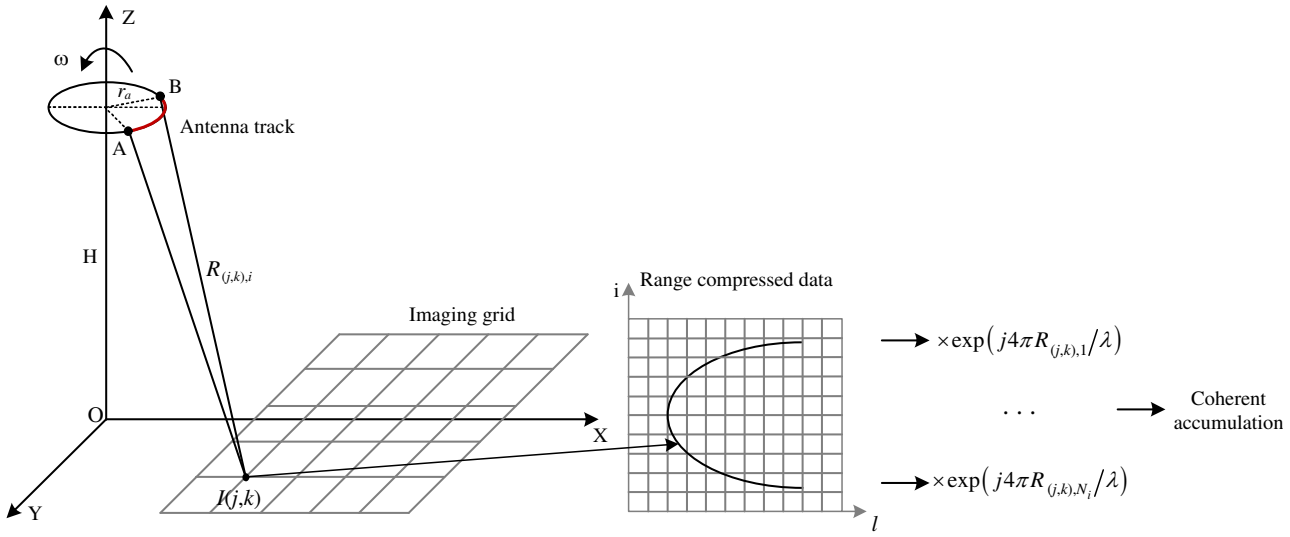

Figure 4. ArcSAR-BP algorithm diagram.

When the imaging grid is established in Cartesian coordinate, the instant slant distance is calculated according to Eq. (1). As a result, the actual ArcSAR image can be obtained. When the imaging grid is established in cylindrical coordinate, the instant slant distance is calculated according to Eq. (3). If the ideal point target is imaged, the imaging result is a two-dimensional sinc function, which can be used for point target analysis.

4.2. Simulation Results

Assuming that the coordinate of the target in both coordinate systems is $P(76,0)$ which is in accordance with the outdoor experiment. The BP algorithm and the system parameters in Table 1 are used to

carry out the simulation. The interpolation multiple N_f in range is 50, resulting in a range step of 0.01 m. Then, 8-point sinc interpolation is applied to obtain coherent accumulation data $S(l, i, N_f)$. Main simulation parameters in two coordinates are summarized in Table 2.

Table 2. Simulation parameters in two coordinates.

Parameters	Cartesian coordinate	Cylindrical coordinate
x-axis	$60 \sim 100\,\mathrm{m}$	$60 \sim 100\,\mathrm{m}$
y-axis	$-20 \sim 20\,\mathrm{m}$	$-0.4 \sim 0.4\,\mathrm{rad}$
X-Sample	501	501
Y-Sample	501	501
Antenna	$(r_a \cos\theta,\ r_a \sin\theta,\ H)$	(ρ, θ, H)

Simulation results are as follows:

Comparing Fig. 5 with Fig. 6, several conclusions can be drawn:

1) Point target response in azimuth of Fig. 5 presents an arc state, which is caused by the circular motion of the antenna. This phenomenon is different from that of linear SAR.
2) The azimuth resolution of the point target in Fig. 5 seems widened. This is the representation of azimuth resolution in different coordinate systems.
3) According to Eq. (14), ArcSAR has a constant azimuth angular resolution and range resolution in cylindrical coordinate system. Therefore, the point target in Fig. 6 is a standard two-dimensional sinc function, which is consistent with the theoretical analysis.

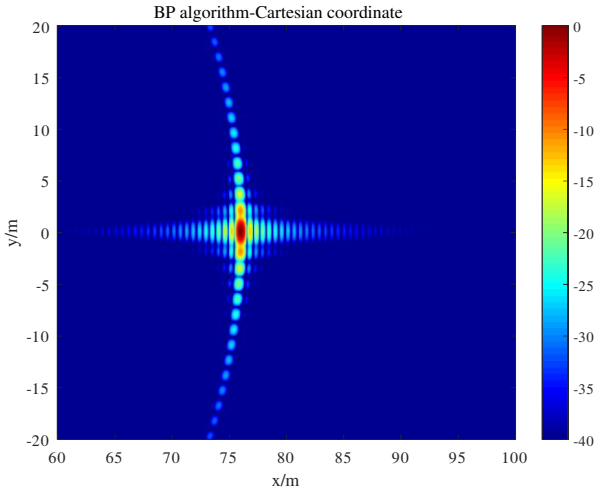

Figure 5. Imaging result in Cartesian coordinate.

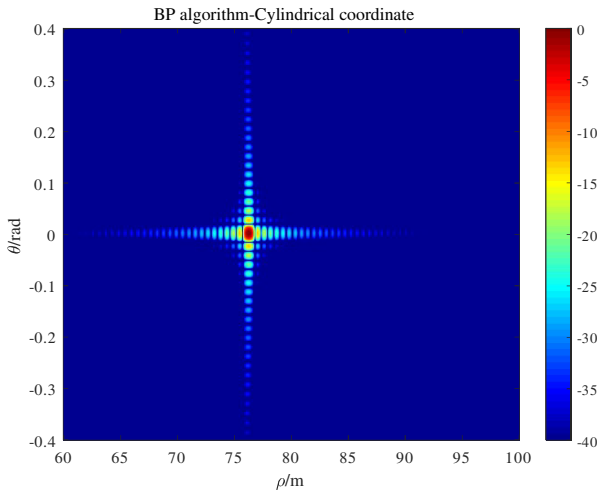

Figure 6. Imaging result in Cylindrical coordinate.

The maximum amplitude pixel of point target is normalized. Centering on the pixel with 0 dB amplitude in Fig. 6, take the 300×140 data matrix around it and perform 16-times FFT-interpolation. Range profile and azimuth profile are shown in Fig. 7 and Fig. 8, respectively:

Point target analysis is summarized in Table 3.

The theoretical azimuth angular resolution without adding window is:

$$\delta_\theta = 0.886 \times \frac{\lambda}{4r_a \cdot \sin(\theta_{BW}/2)} = 0.0156\,\mathrm{rad} \tag{16}$$

The theoretical value of azimuth angular resolution is consistent with the simulation result. PSLR and ISLR are both meet the standard of SAR image quality parameters. The point target response

Table 3. Point target analysis.

Parameters	Range	Azimuth
IRW	0.48 m	0.0155 rad
PSLR	−13.25 dB	−13.2 dB
ISLR	−10.1415 dB	−10.1422 dB

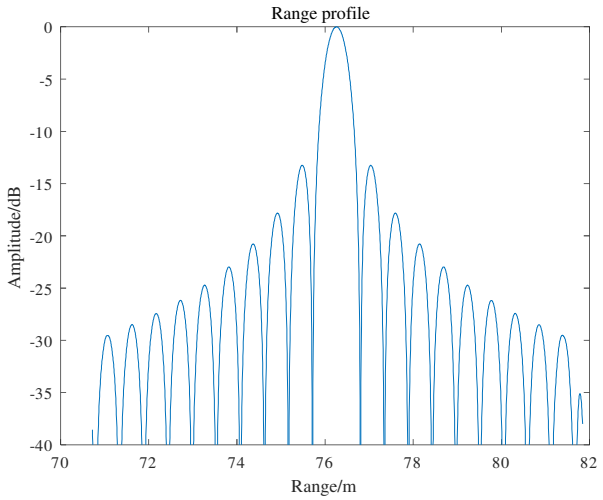

Figure 7. Simulation range profile.

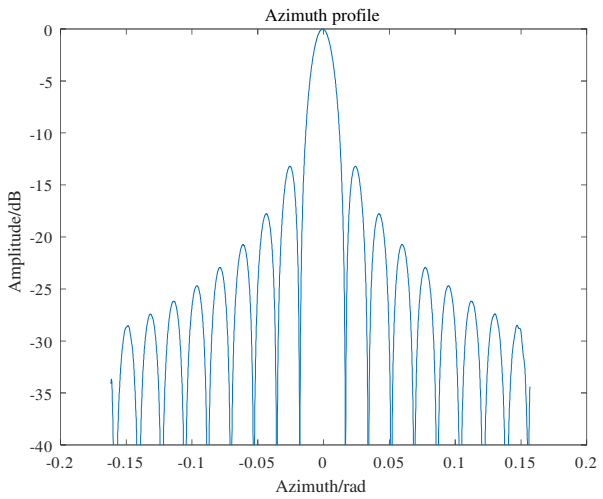

Figure 8. Simulation azimuth profile.

presents a 2-dimensional sinc function in cylindrical coordinate, and the point target analysis should be calculated in cylindrical coordinate.

5. EXPERIMENTAL RESULT

5.1. Experimental Scene

The ArcSAR system was placed on a terrace on the top floor of the experimental building in NSSC. The rotating arm is extended out of the building during the experiment. A corner reflector was placed in the center of the scene, marked by a red circle in Fig. 9. Since there are many tree trunks on the ground surface, in order to avoid the strong reflection of the trunks, the HH-polarized antenna is adopted. The nearest distance R_0 between corner reflector and antenna is about 83 m, and r_p is about 76 m. The experimental scenario is shown in Fig. 9.

5.2. Result and Analysis

5.2.1. Image of Corner Reflector

Imaging geometry is set up as Fig. 4. The same parameters in Table 2 are used to process the raw data of ArcSAR, so the point target analysis of measured data and simulated data can be compared. The imaging results in Cartesian coordinate and cylindrical coordinate are shown in Fig. 10 and Fig. 11, respectively.

From two ArcSAR images, the characteristics in the two coordinates are summarized as follows:

1) Different from the simulation results, the azimuth sidelobe levels are reduced due to the weighting of antenna pattern. The reasons that the antenna pattern has not been imposed on simulation results are that the simulated antenna pattern is an ideal sinc-like function. However, in the real experiment, the antenna pattern is affected by various factors, and the shape will not be the ideal

Figure 9. Experiment scenario.

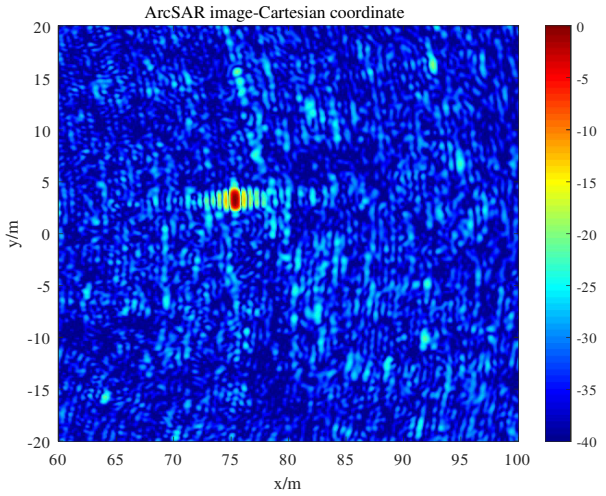

Figure 10. Image of reflector in Cartesian coordinate.

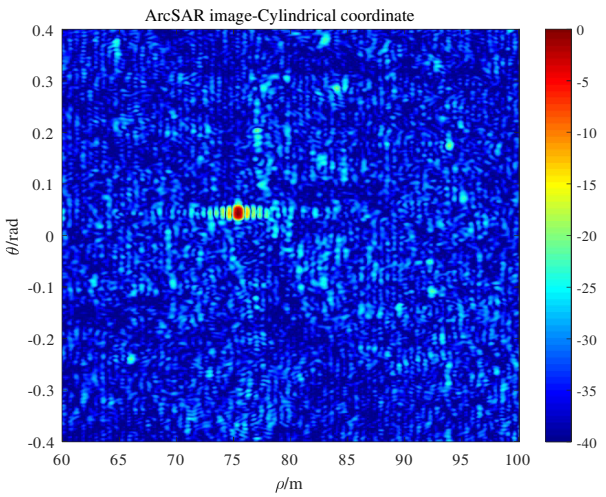

Figure 11. Image of reflector in Cylindrical coordinate.

sinc-like function. Accordingly, the azimuth signal of the corner reflector and the simulated azimuth signal will not match perfectly. Besides, the image of the simulated point target without antenna pattern is a standard two-dimensional sinc function (see Fig. 6) which can be used for the point target analysis. The validity of the algorithm can be proved quantitatively. Window function has not been imposed on range data, so the range sidelobes are clear in both figures.

2) The azimuth resolution in Cartesian coordinate seems widened too which is consistent with simulation result (Fig. 5).

5.2.2. Point Target Analysis

Similarly, the maximum amplitude pixel of point target is normalized. In cylindrical coordinate, taking the pixel with 0 dB amplitude as the center, a 200×140 matrix around the pixel is selected, and 16-times interpolation is applied to analyze typical parameters. Range profile and azimuth profile are shown in Figs. 12–13.

Point target analysis of measured data is calculated in Table 4.

Under the experimental parameters listed in Table 1, the theoretical range resolution is:

$$\delta_r = 0.886 \times \frac{c}{2N\Delta f} = 0.443\,\mathrm{m} \tag{17}$$

Table 4. Point target analysis of measured data.

Parameters	Range	Azimuth
IRW	0.49 m	0.0175 rad
PSLR	−12.45 dB	−22.32 dB
ISLR	−9.5842 dB	−19.2216 dB

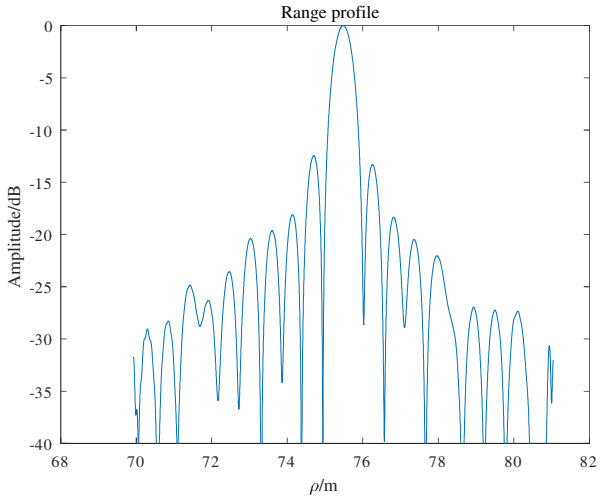

Figure 12. Range profile of corner reflector.

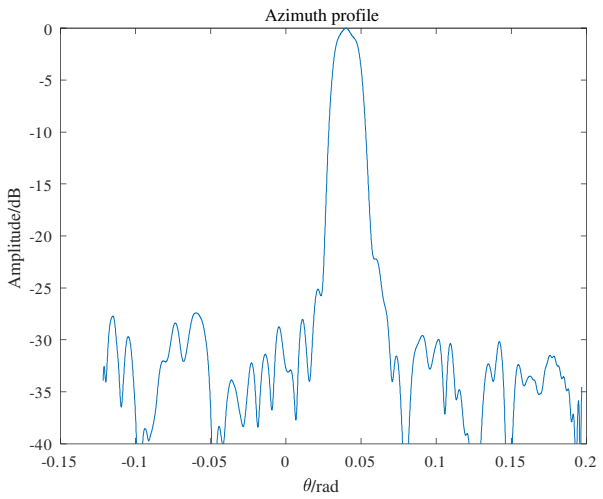

Figure 13. Azimuth profile of corner reflector.

Since measured azimuth signal is weighted by the antenna pattern, the coefficient of azimuth angular resolution can be negligible. The formula of azimuth angular resolution is updated as [26]:

$$\delta_{\theta wind} = \frac{\lambda}{4r_a \cdot \sin(\theta_{BW}/2)} = 0.0176\,\text{rad} \tag{18}$$

The measured range resolution differs from the theoretical value by 0.047 m, and the measured azimuth angular resolution is identical with the theoretical value. ArcSAR-BP algorithm relies on high-precision instant distance calculation, but there are some random error factors in outdoor experiment that will cause certain deviation between measured distance and theoretical distance such as: additional random vibration of antenna caused by strong wind and error of laser rangefinder. Regardless of error factors, it is considered that the theoretical value is consistent with the measured value, which proves the effectiveness of ArcSAR system and BP algorithm.

6. CONCLUSIONS

In this paper, an SFCW-ArcSAR system is developed. The raw signal model and signal properties of ArcSAR were deduced. Based on simulation and outdoor experiment with corner reflector, the point target responses of ArcSAR in both Cartesian coordinate and cylindrical coordinate are investigated. The results count for subsequent application of ArcSAR. Based on the comparative analysis of theory, simulated and measured data, the following conclusions are drawn:

1) The azimuth angular resolution of ArcSAR is independent of range. The larger the length of the rotating arm and beamwidth are, the finer the azimuth angular resolution is.
2) The point target response of ArcSAR is a two-dimensional sinc function in cylindrical coordinate system, so the point target analysis should be carried out in this coordinate.
3) The theatrical azimuth angular resolution and simulated results of the system are highly consistent with the measured results, which proves the effectiveness of SFCW-ArcSAR system.

The result in this paper can be used to verify other algorithms proposed for ArcSAR. ArcSAR has the advantages of large field of view and constant azimuth angular resolution, which will have a good application prospect in regional mapping or environmental monitoring.

ACKNOWLEDGMENT

This work was supported by the Science and Technology Research and Development Program of China National Railway Corporation Limited K2019G007.

REFERENCES

1. Monserrat, O., M. Crosetto, and G. Luzi, "A review of ground-based SAR interferometry for deformation measurement," *ISPRS Journal of Photogrammetry & Remote Sensing*, Vol. 93, 40–48, 2014.
2. Pieraccini, M. and L. Miccinesi, "Ground-based radar interferometry: A bibliographic review," *Remote Sensing*, Vol. 11, No. 9, 1029, 2019.
3. Wang, Y., W. Hong, Y. Zhang, et al., "Ground-based differential interferometry SAR: A review," *IEEE Geoscience and Remote Sensing Magazine*, Vol. 8, No. 1, 43–70, 2020.
4. Frodella, W., A. Ciampalini, F. Bardi, et al., "A method for assessing and managing landslide residual hazard in urban areas," *Landslides*, Vol. 15, 183–197, 2018.
5. Pieraccini, M., N. Rojhani, and L. Miccinesi, "Compressive sensing for ground based synthetic aperture radar," *Remote Sensing*, Vol. 10, No. 12, 1960, 2018.
6. Luzi, G., M. Pieraccini, D. Mecatti, et al., "Monitoring of an alpine glacier by means of ground-based SAR interferometry," *IEEE Geoscience and Remote Sensing Letters*, Vol. 4, No. 3, 495–499, 2007.
7. Nico, G., G. Prezioso, O. Masci, and Y. Izumi, "Monitoring strategies of displacements and vibration frequencies by ground-based radar interferometry," *Communications in Computer and Information Science*, Vol. 1246, 379–374, 2019.
8. Calvari, S., E. Intrieri, F. D. Traglia, et al., "Monitoring crater-wall collapse at active volcanoes: A study of the 12 January 2013 event at Stromboli," *Bulletin of Volcanology*, Vol. 78, No. 5, 1–16, 2016.
9. Pieraccini, M. and L. Miccinesi, "An interferometric MIMO radar for bridge monitoring," *IEEE Geoscience and Remote Sensing Letters*, Vol. 16, No. 9, 1383–1387, Sept. 2019.
10. Tarchi, D., F. Oliveri, and P. F. Sammartino, "MIMO radar and ground-based SAR imaging systems: Equivalent approaches for remote sensing," *IEEE Transactions on Geoscience & Remote Sensing*, Vol. 51, No. 1, 425–435, 2013.
11. Ponce, O., et al., "Fully polarimetric high-resolution 3-D imaging with circular SAR at L-band," *IEEE Transactions on Geoscience and Remote Sensing*, Vol. 52, No. 6, 3074–3090, Jun. 2014.
12. Jia, G., W. Chang, Q. Zhang, and X. Luan, "The analysis and realization of motion compensation for circular synthetic aperture radar data," *IEEE Journal of Selected Topics in Applied Earth Observations and Remote Sensing*, Vol. 9, No. 7, 3060–3071, Jul. 2016.
13. Viviani, F., A. Michelini, L. Mayer, and F. Conni, "IBIS-ArcSAR: An innovative ground-based SAR system for slope monitoring," *IGARSS 2018 — 2018 IEEE International Geoscience and Remote Sensing Symposium*, 1348–1351, 2018.
14. Michelini, A., F. Viviani, and L. Mayer, "Introduction to IBIS-ArcSAR: A circular scanning GB-SAR system for deformation monitoring," *Proceedings of the 4th Joint International Symposium on Deformation Monitoring (JISDM)*, 15–17, Athens, Greece, 2019.
15. Lee, H., J. Lee, K. Kim, N. Sung, and S. Cho, "Development of a truck-mounted Arc-scanning synthetic aperture radar," *IEEE Transactions on Geoscience and Remote Sensing*, Vol. 52, No. 5, 2773–2779, May 2014.

16. Luo, Y., H. Song, R. Wang, Y. Deng, F. Zhao, and Z. Xu, "Arc FMCW SAR and applications in ground monitoring," *IEEE Transactions on Geoscience and Remote Sensing*, Vol. 52, No. 9, 5989–5998, Sept. 2014.
17. Lin, Y., Y. Liu, Y. Wang, S. Ye, Y. Zhang, Y. Li, W. Li, H. Qu, and W. Hong, "Frequency domain panoramic imaging algorithm for ground-based ArcSAR," *Sensors*, Vol. 20, No. 24, 7027, 2020.
18. Pieraccini, M., G. Luzi, and C. Atzeni, "Terrain mapping by ground-based interferometric radar," *IEEE Transactions on Geoscience and Remote Sensing*, Vol. 39, No. 10, 2176–2181, Oct. 2001.
19. Desai, M. D. and W. K. Jenkins, "Convolution backprojection image reconstruction for spotlight mode synthetic aperture radar," *IEEE Transactions on Image Processing*, Vol. 1, No. 4, 505–517, Oct. 1992.
20. Ulander, L. M. H., H. Hellsten, and G. Stenstrom, "Synthetic-aperture radar processing using fast factorized back-projection," *IEEE Transactions on Aerospace and Electronic Systems*, Vol. 39, No. 3, 760–776, Jul. 2003.
21. Iker, H. and C. Zdemir, "Adaptation of stepped frequency continuous waveform to range-Doppler algorithm for SAR signal processing," *Digital Signal Processing*, Vol. 106, No. 4, 102826, 2020.
22. Soumekh, M., *Synthetic Aperture Radar Signal Processing with MATLAB Algorithms*, 1999.
23. Hanssen, R., R. Bamler, et al., "Evaluation of interpolation kernels for SAR interferometry," *IEEE Transactions on Geoscience & Remote Sensing*, Vol. 37, No. 1, 318–321, 1999.
24. Pieraccini, M. and L. Miccinesi, "ArcSAR: Theory, simulations, and experimental verification," *IEEE Transactions on Microwave Theory and Techniques*, Vol. 65, No. 1, 293–301, Jan. 2017.
25. Yigit, E., "Short-range ground-based synthetic aperture radar imaging: Performance comparison between frequency-wavenumber migration and back-projection algorithms," *Journal of Applied Remote Sensing*, Vol. 7, No. 1, 073483, 2013.
26. Cumming, I. G. and F. H. Wong, *Digital Signal Processing of Synthetic Aperture Radar Data: Algorithms and Implementation*, 2004.